

# Synthetic neutrino imaging of a microquasar

Theodoros Smponias<sup>1</sup>

*Directorate of Secondary Education of the Dodekanese, Rhodes, Greece*

---

## Abstract

Particle emission from simulated twin microquasar jets is calculated in a unified manner. A program suite assembled around model data produces synthetic images and spectra, directly comparable to potential observations by contemporary arrays. The model is capable of describing a multitude of system geometries, incorporating increasing levels of realism, depending on the needs and on available computational resources. As an application, the modelling process is applied to a typical microquasar, which is synthetically observed from five different angles and with different imaging geometries.

*Keywords:*

ISM: jets and outflows, stars: winds-outflows, stars: flare, radiation  
mechanisms: general, methods: numerical

*2010 MSC:* 85-08

---

## 1. Introduction

Microquasars (MQ) comprise a binary stellar system where a main sequence star orbits a compact object, either a neutron star or a black hole [1]. Matter from the star accretes onto the collapsed stellar remnant, resulting to the  
5 production of twin relativistic jets, pointing in opposite directions. Those jets emit over a broad spectrum, from radio to very high energy (VHE)  $\gamma$ -rays and neutrinos [2], [3], [4], [5], [6]).

---

\*Corresponding author

*Email address:* t.smponias@hushmail.com (Theodoros Smponias)

As mentioned in [2], apparent superluminal motion in certain MQ indicate the presence of bulk hadron flows in the jets. The assumption of equipartition  
10 [5], leads to high magnetic field estimates for the jet [7]. This, coupled with the fluid approximation for the jet matter, due to the presence of tangled magnetic fields [8] [9], allows the magneto-hydrodynamic (MHD) approximation for the jets. A toroidal magnetic field component may retain jet collimation over considerable distances along its path [7] [10].

15 In this paper, the production of very high energy (VHE) neutrinos from generic MQ jets is modelled, using the method of dynamic and radiative relativistic MHD simulation. The paper is organized as follows:

In Section 2 the theoretical background of the work is presented. In Section 3 is obtained the emission of particles from the jet. In Section 4 the results are  
20 presented and discussed. The normalization/equipartition (and the synthetic imaging process) are described in the Appendix.

## 2. Theoretical setup

In our generic MQ model, an accretion disk is assumed around the compact object [11]. Twin jets emanate from the vicinity of the collapsed star, collimated  
25 by a toroidal magnetic field component. Adopting a heavier pair of jets, their kinetic power is set to  $L_k = 2 \times 10^{38}$  (see Appendix). [5] argue a 10 percent Eddington luminosity jet power, leading to  $L_k = 10^{38} \text{ ergs}^{-1}$  for a  $10 M_\odot$  black hole, which is comparable to our simulation. Furthermore, the same authors argue either  $\frac{L_p}{L_e} \simeq 100$  or  $\simeq 1$ , and in our case we shall adopt the former hypothesis, favouring protons. Equipartition means  $\rho_k = \rho_B$ , therefore  $B(z) = \sqrt{8\pi\rho_z}$   
30 [8] [9], a close match with the B used in the simulation (see Appendix).

### 2.1. Non-thermal proton density

Neutrino emission from the jets is taken to originate from proton-proton interaction between a distribution of hot (fast) protons and cold (bulk flow)  
35 protons [2, 4, 5, 6, 12, 13]. Some of the bulk protons get accelerated at shock

fronts, according to the first order Fermi acceleration mechanism, with a time scale of [14], [8], [9]

$$t_{acc}^{-1} \simeq \eta \frac{ceB}{E_p}, \quad (1)$$

where  $B$  is the magnetic field and  $E_p$  the proton energy,  $e$  being the proton charge and  $c$  the speed of light.  $\eta = 0.1$  represents an acceleration efficiency parameter, assuming efficient acceleration in moderately relativistic shocks in the vicinity of the jet base [14].

In the present work, we adopt a power-law distribution, for the fast protons, of the form  $N_p = N_0 E^{-\alpha}$  [15], with either  $\alpha \approx 2$  [4], or a variable  $\alpha$  [6], where  $\alpha$  is the proton spectral index in the local jet cell matter frame. Alternatively, a transport equation could be used to find the distribution [4].

As a further approximation, the aforementioned hot proton distribution is taken to be isotropic in the jet frame, assuming the scattering length  $l_{sc}$  is less than the radiative length,  $l_r$ , a hypothesis backed by the nature of diffuse shock acceleration [16].

## 2.2. A note on jet frame anisotropy

For protons accelerated at diffuse shocks, the above assumption of isotropy goes by definition, since at shocks it has to preserve, after every bounce, at least some  $E$ , therefore  $l_{sc}$  is clearly less than  $l_r$ , else it would not have any  $E$  left after the bounce!

According to [16], an assumed anisotropy of the hot proton distribution can be reflected to the neutrino distribution. In the jet system, emission would then be projected off axis, even reinforced, under certain orientations, in the lab frame.

## 3. Neutrino emission calculations

### 3.1. Proton energy loss

Following [12], [5], and [6], certain energy loss mechanisms are included. This presentation is performed at a cell with the properties

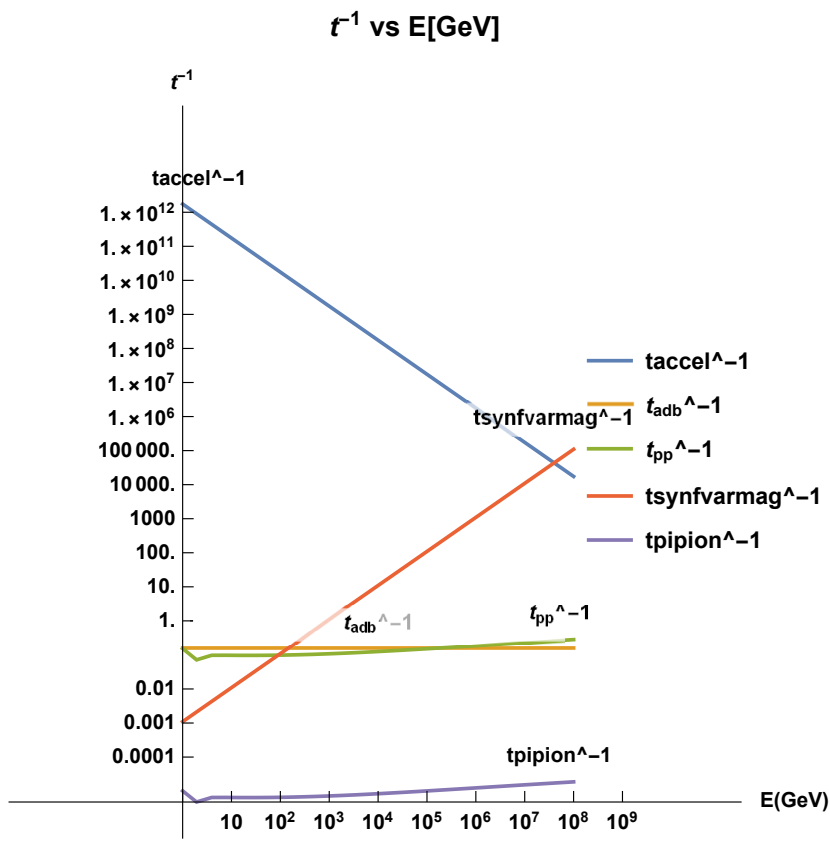


Figure 1: High energy proton distribution loss time scales, for various processes in the jets, plotted with energy in erg.  $t_{pion}$  stands for the pion decay timescale  $t_\pi$ .

of:  $(u_x, u_y, u_z, b_x, b_y, b_z, n_p, \phi_1, \phi_2, \alpha) = (-0.3780c, 0.4480c, 0.0124c, 10^5G, 10^6G, 10^5G, 2.1 \times 10^{11}cm^{-3}, 1.047 \text{ rad}, 5.00 \times 10^{-7}rad, 2.0)$ . Nevertheless, in the  
65 model runs these are potentially performed in every cell.

We consider a cutoff maximum E for protons of  $E_{max}=10^6$  GeV. For the adiabatic expansion time scale we have [5]

$$t_{adb}^{-1} = \frac{2}{3} \frac{u_{b(adb)}}{z_j} \quad (2)$$

where  $z_j=10^{11}$  cm is the characteristic lateral size scale of the jet. For this simple calculation,  $u_{b(adb)}$  is preset to 0.8. For the p-p collision loss mechanism, we have

$$t_{pp}^{-1} = nc\sigma_{inel_{pp}}(E_p)K_{pp} \quad (3)$$

$$\sigma_{pp}^{(inel)} = (34.3 + 1.88L + 0.25L^2) \times [1 - (\frac{E_{th}}{E_p})^4]^2 \times 10^{-27}cm^2 \quad (4)$$

$\sigma_{pp}^{inel}$  is the inelastic p-p scattering cross section.

For the pion decay time we have

$$t_{\pi 0} = 2.6 \times 10^{-8}s \quad (5)$$

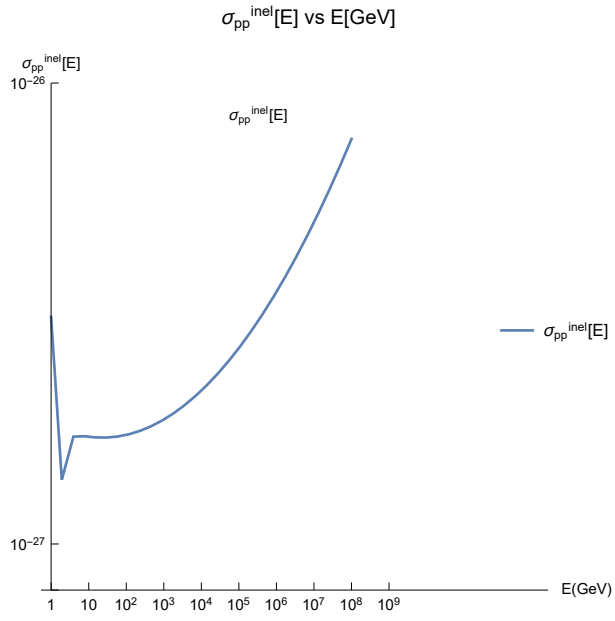


Figure 2: Inelastic proton-proton collision standard plotted with energy.  
**ndens\_cutoff vs E[GeV] @Ecutoff=1.3\*e12 GeV**

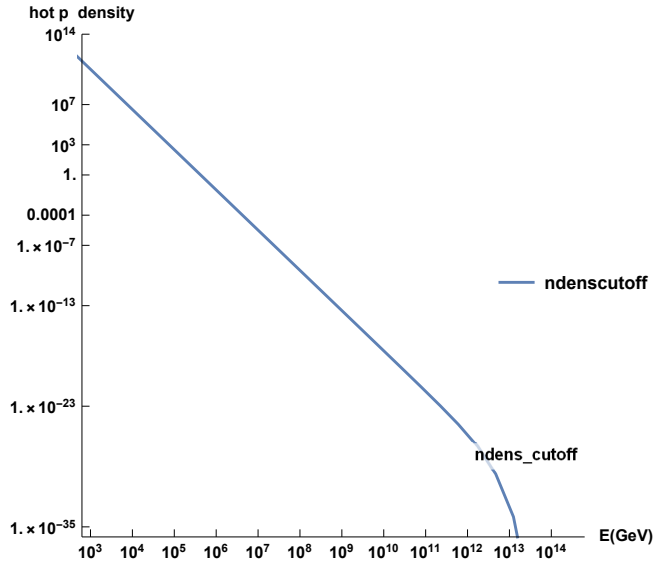


Figure 3: The density of non-thermal protons in the jet is plotted with energy.

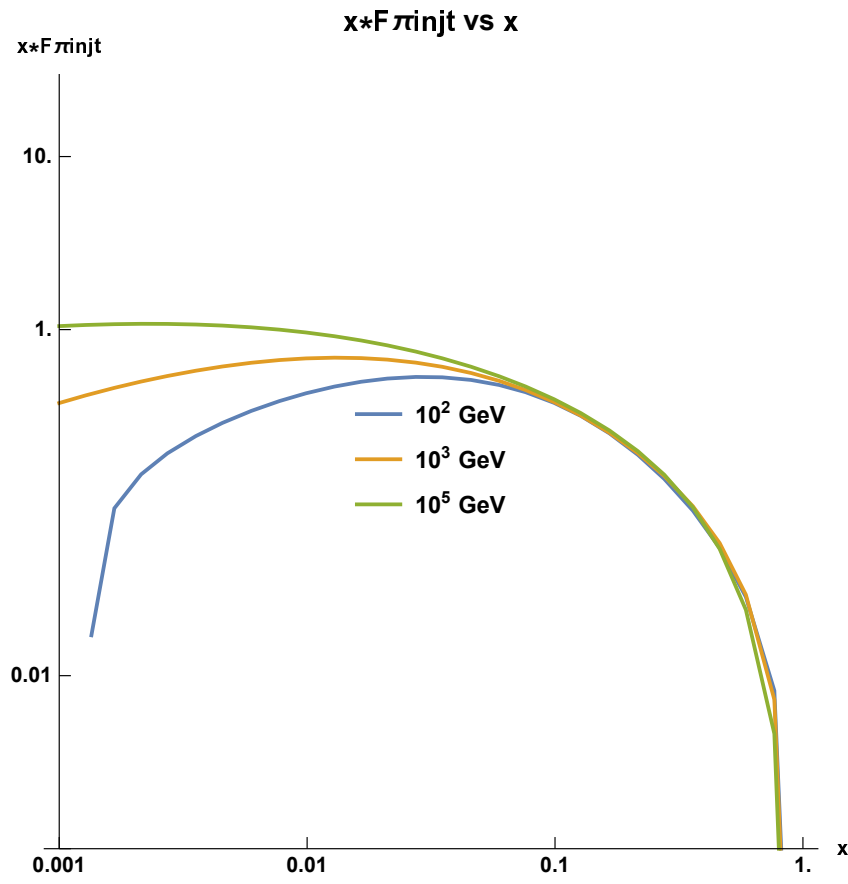


Figure 4: The F function, corresponding to the pion spectrum emerging from a single (hot-cold) proton collision, is presented here, multiplied by the  $x=\frac{E_\pi}{E_p}$  fraction. The calculation is performed at three different energies for the non-thermal proton.

and

$$t_\pi = t_{\pi 0} \Gamma_\pi + t_{esc} \quad (6)$$

which in practice takes the form

$$t_\pi = t_{\pi 0} \left( \frac{E_\pi}{m_\pi c^2} \right) + t_{esc} \quad (7)$$

where the light escape time  $t_{esc}$  strongly affects the final result.

The synchrotron loss time scale is defined by

$$t_{sync}^{-1} = \frac{4}{3} \left( \frac{m_e}{m_p} \right)^3 \frac{1}{8\pi c m_e} \sigma_T B^2 \frac{E_p}{m_p c^2} \quad (8)$$

The form of the latter term, which is essentially  $\Gamma_p$ , facilitates energy-dependent calculations later-on. In total

$$t_{loss}^{-1} = t_{sync}^{-1} + t_{adb}^{-1} + t_{pp}^{-1} \quad (9)$$

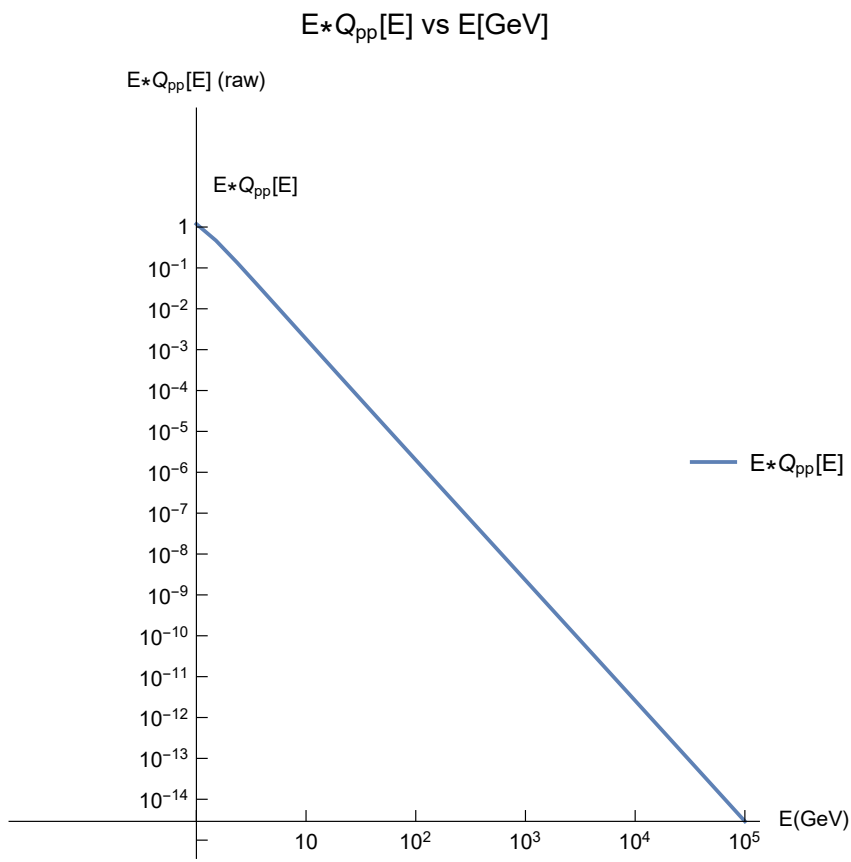


Figure 5: The function  $Q$ , describing the combined spectrum from a multitude of (hot-cold) p-p collisions, spanning a range from 1 GeV to 100000 GeV.

### 3.2. A model for the interaction of thermal and non-thermal protons in the jet.

Hot-cold proton interaction results to a distribution of high energy pions, which then decay allowing the creation of energetic neutrinos. We have [17, 18, 19]

$$pp \rightarrow pp\pi^0 + \pi_0, \quad (10)$$

for neutral pions  $\pi^0$  and

$$pp \rightarrow pn\pi^+ + \pi_+, \quad pp \rightarrow pn\pi^- + \pi_-, \quad (11)$$

for  $\pi^\pm$ .

$\pi^0$  decay to gamma-rays, while  $\pi^\pm$  mostly to an anti-muon or muon and a muonic neutrino or anti-neutrino (prompt neutrinos) [17].

$$\pi^+ \rightarrow \mu^+ + \nu_\mu, \quad \pi^- \rightarrow \mu^- + \tilde{\nu}_\mu. \quad (12)$$

As an approximation, we neglect both neutrino production through secondary channels and delayed neutrinos.

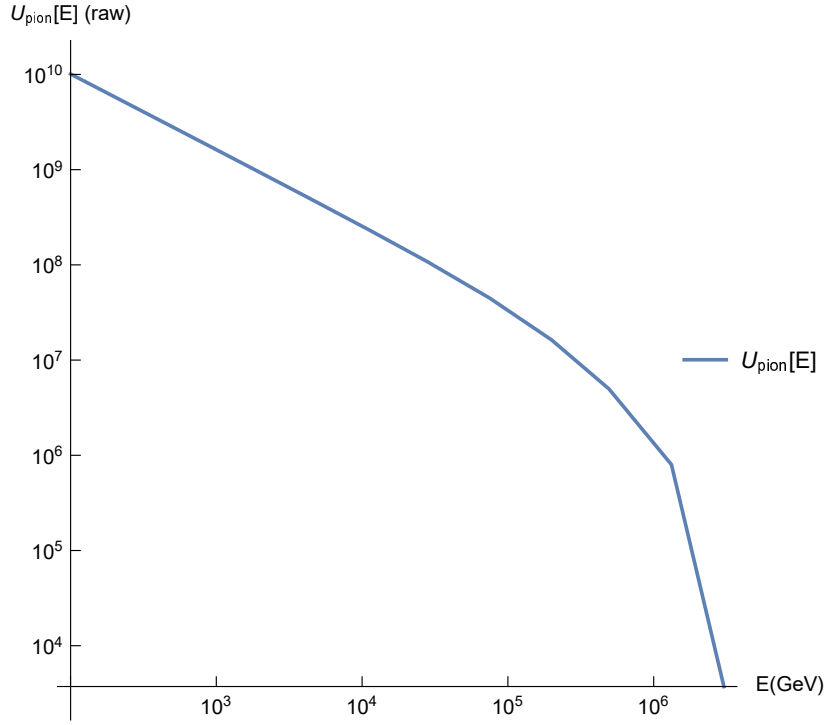


Figure 6: Pion energy distribution, plotted in non-normalized units versus energy.

For each successive particle population in the above cascades, the transport  
 75 equation [20] can be solved. Nevertheless, for protons a power-law distribution  
 is assumed, skipping having to solve the first transport equation in the cascade.  
 From protons to pions then to muons and neutrinos, each generation of particles  
 leads to the next one. [12] calculate the properties of resulting particle distribu-  
 tions over a large energy range, performing Monte Carlo calculations with the  
 80 results of particle physics.

In previous works [19, 21, 22], the hadronic jet was modelled using the  
 PLUTO code. The results of PLUTO were then processed in order to cal-  
 culate the emissivity of  $\gamma$ -rays and neutrino using various approximations. In  
 this paper, the neutrino emissivity is calculated separately at each spatial com-  
 85 putational cell, using the angle  $(\cos\theta)$ , formed between the LOS and the local  
 velocity.

### 3.3. Lorentz transform of high $E$ proton distribution

For the calculation of the fast proton distribution, the relevant directional  
 equation is found in [23] [24]. The latest variant originates from [23], used here,



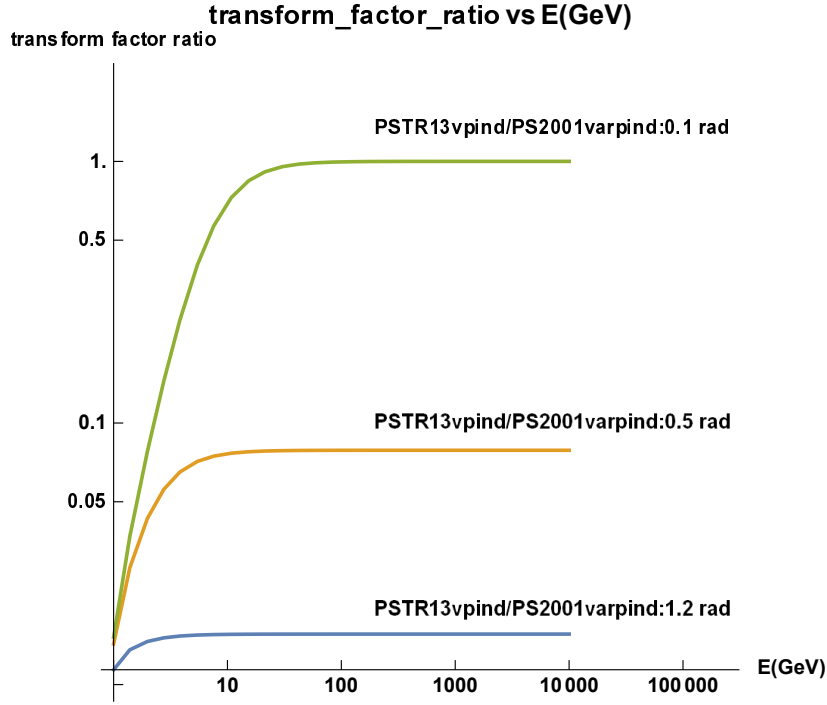


Figure 7: The ratio of TR13/PS01 HE proton distribution density transformation, for three different angles. A reproduction, for verification, of a figure from [23].

minus a geometry factor that we absorb into the normalization factor

$$n(E, \theta) = \frac{\Gamma^{-\alpha-1} E^{-\alpha} (1 - \beta \cos(\theta)) \sqrt{1 - \frac{m^2 c^4}{E^2}}^{-\alpha-1}}{[\sin^2(\theta) + \Gamma^2 (\cos(\theta) - \frac{\beta}{\sqrt{1 - \frac{m^2 c^4}{E^2}}})^2]^{\frac{1}{2}}} \quad (13)$$

On the other hand, [24] say

$$n(E, \theta) = \frac{\Gamma^{-\alpha+1} E^{-\alpha} (1 - \beta \cos(\theta)) \sqrt{1 - \frac{m^2 c^4}{E^2}}^{-\alpha}}{[\sin^2(\theta) + \Gamma^2 (\cos(\theta) - \frac{\beta}{\sqrt{1 - \frac{m^2 c^4}{E^2}}})^2]^{\frac{1}{2}}} \quad (14)$$

And a simpler variant [21]

$$n(E, \theta) = \Gamma(E - \beta \sqrt{E^2 - m^2 c^4} \cos(\theta)) \quad (15)$$

The above are plotted in Figures 7, 8 and 9.

### 3.4. Pion injection function and pion energy distribution

90 For each fast-slow proton interaction a spectrum of possible pion energies exists, given by the function  $F_\pi$  ([12], [5] and [6]).

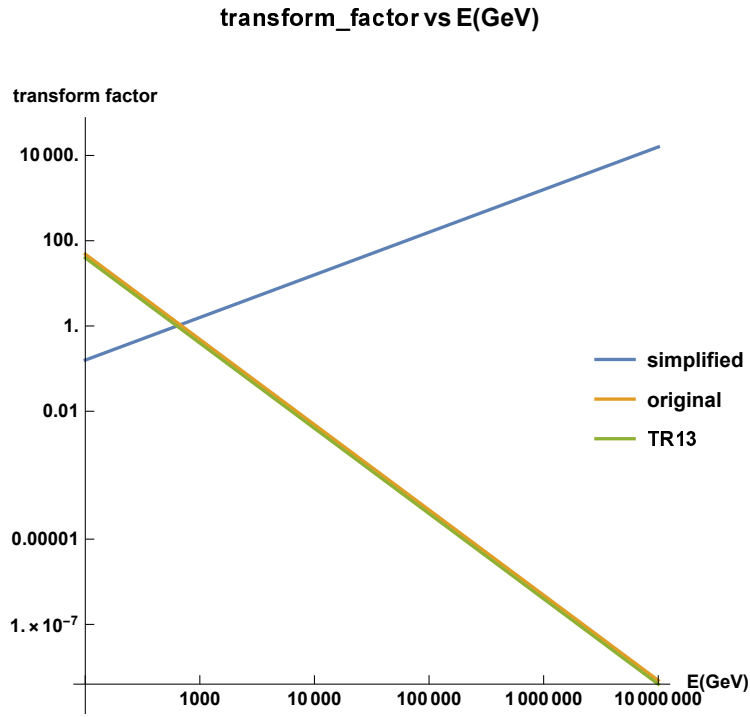


Figure 8: Three different expressions used for non-thermal proton distro transform, plotted with energy.

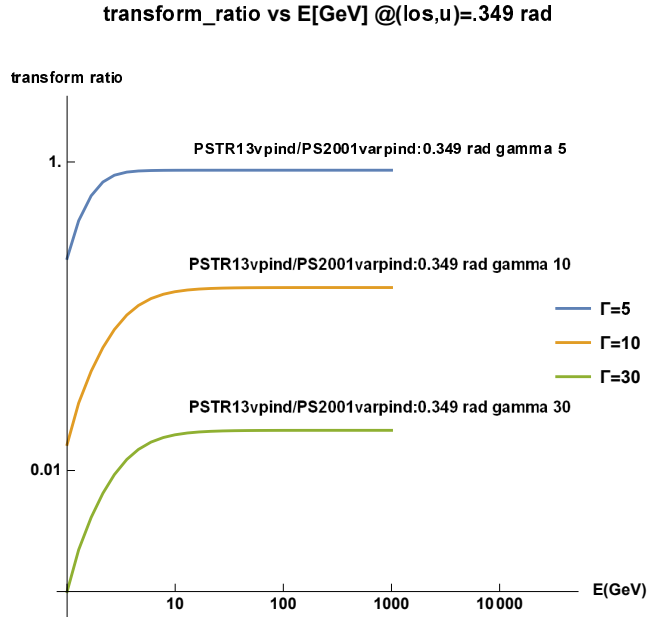


Figure 9: The ratio of TR13/PS01 non-thermal proton distribution density transformation, for three different Lorentz factors. A reproduction, for verification, of a figure from [23].

$$F_{\pi}^{(pp)}\left(x, \frac{E}{x}\right) = 4\alpha B_{\pi} x^{\alpha-1} \left(\frac{1-x^{\alpha}}{1+rx^{\alpha}(1-x^{\alpha})}\right)^4 \left(\frac{1}{1-x^{\alpha}} + \frac{r(1-2x^{\alpha})}{1+rx^{\alpha}(1-x^{\alpha})}\right) \left(1 - \frac{m_{\pi}c^2}{xE_p}\right)^{\frac{1}{2}} \quad (16)$$

where  $x = E/E_p$ , and  $L = \ln(E_p/1000\text{GeV})$ ,  $E_{th} = 1.2 \text{ GeV}$  (see [5, 12]).

In Fig. 2  $\sigma_{pp}^{(inel)}$  is plotted. In Fig. 3 the p-law fast proton density is shown.

In Fig. 4  $xF_{\pi}$  is plotted with the fraction  $x$  for different fast proton energies.

95 The pion injection function,  $Q_{\pi}^{(pp)}$ , comprises, at each pion energy, pion contributions, to that pion energy, from the spectrum F, of all potential p-p interactions.

$$Q_{\pi}^{(pp)}(E, z) = n(z)c \int_{\frac{E}{E_p^{(max)}}}^1 \frac{dx}{x} \left(\frac{E}{x}, z\right) F_{\pi}^{(pp)}\left(x, \frac{E}{x}\right) \sigma_{pp}^{(inel)}\left(\frac{E}{x}\right), \quad (17)$$

$x$  is the fraction of the pion energy to proton energy, and  $n(z)$  is the jet flow proton density.

100 In Fig 5  $Q_{\pi}^{(pp)}$  is plotted versus the pion energy  $E_{\pi}$ .

In order to obtain the pion distribution, we solve the following transport equation

$$\frac{\partial N_{\pi}}{\partial E} + \frac{N_{\pi}}{t_{loss}} = Q_{\pi}^{(pp)}(E, z) \quad (18)$$

where  $N_{\pi}(E, z)$  denotes the pion energy distribution. We proceed

$$N_{\pi}(E) = \frac{1}{|b_{\pi}(E)|} \int_E^{E^{(max)}} dE' Q_{\pi}^{(pp)}(E') \exp[-\tau_{\pi}(E, E')], \quad (19)$$

where

$$\tau_{\pi}(E', E) = \int_{E'}^E \frac{dE'' t_{\pi}^{-1}(E'')}{|b_{\pi}(E'')|}. \quad (20)$$

The above are performed for each computational cell, where quantities, for radiative purposes, are considered locally constant. A cell is macroscopically large,

105 inasmuch only the deterministic portion of the transport equation is employed,  
in turn rendering it deterministic. Again we take the characteristic scale (mean  
free path) of the radiative interactions to be smaller than the cell size, lead-  
ing to the containment of particle interactions within a given hydrocode cell.  
Furthermore, the time scale for the radiative interactions is taken to be smaller  
110 enough than the hydrocode's timestep, that the radiative interactions belong to  
a single timestep each time.

### 3.5. Neutrino emissivity

The emissivity of prompt neutrinos [12, 13, 4, 5], is

$$Q_{\pi \rightarrow \nu}(E) = \int_E^{E_{max}} dE_\pi t_\pi^{-1}(E_\pi) N_\pi(E_\pi) \frac{\Theta(1 - r_\pi - x)}{E_\pi(1 - r_\pi)}, \quad (21)$$

$x = E/E_\pi$  and  $t_\pi$  is the pion decay timescale.  $\Theta(\chi)$  is the theta function [5, 19].

115 Neutrino emissivity is calculated for each individual cell, using the cell's own  
angle to the LOS crossing that cell. The imaging process may either incorporate  
parallel LOS's or a focused beam, where each LOS follows a slightly different  
path to a common focal point [25]. A synthetic image of the model system is  
thus produced.

## 120 4. Results and discussion

### 4.1. Model setup

The jet base is situated near the centre of a Cartesian XYZ grid. A con-  
tinuous model jet, representing a microquasar system, injected at  $u_{jet} = 0.865c$   
is studied with the RMHD setup of the PLUTO hydrocode, at a uniform grid  
125 resolution of  $60 \times 100 \times 50$ . In all of the model runs the same initial jet density  
of  $10^{10}$  protons/cm<sup>3</sup> is used, 2000 times less than the maximum surrounding gas  
density. Winds comprise an accretion disk wind construct and a stellar wind,  
which falls off away from the companion star, located off-grid at (400, 100, 400),  
while the jet is threaded by a strong confining toroidal magnetic field of  $B=10^4$

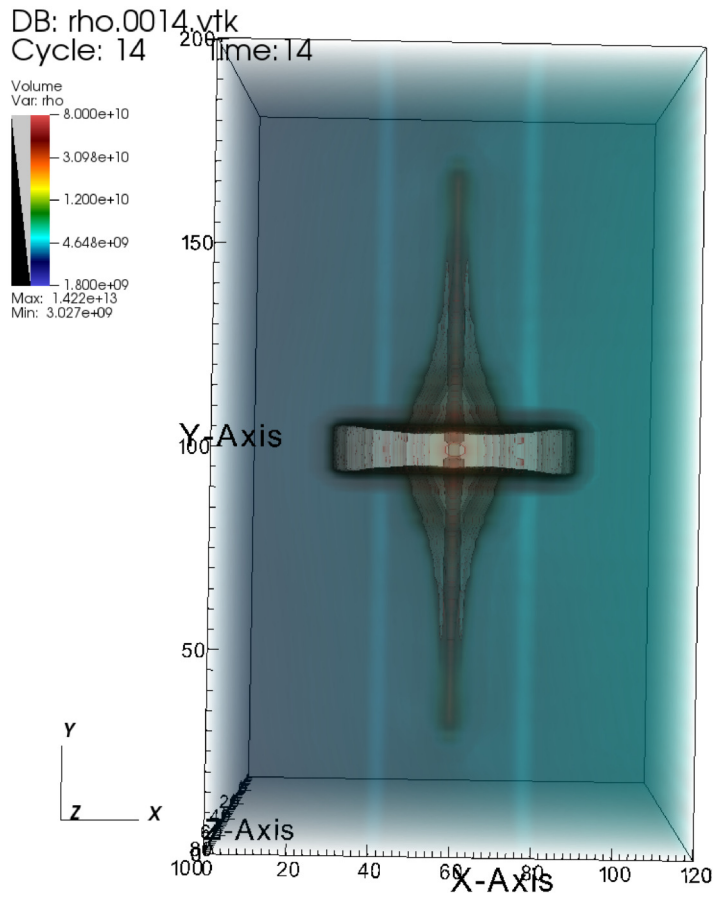


Figure 10: Snapshot 14 of the  $u=0.866c$  hydrocode run, corresponding to a model time of  $t=350$  ( $14 \times 25$ ), depicting the density in a logarithmic plot. We can see both jet fronts advancing towards the ends of the grid, traversing the surrounding stellar wind, after crossing the simplified accretion disk wind construct. Image produced with VisIt.

130 G. The simulations were run until  $t = 842$  s, saving a data snapshot every 25 time units. A snapshot of density is shown in Figures 10 and 11, in 3D and 2D respectively, where we can see the magnetically collimated jet pair advancing through surrounding winds.

A number of empty user parameters were fully employed, in order to house particle emission results later on. Then, the above PLUTO run was copied into  
 135 many directories. In each one of them, the nemiss program [26] was run, that calculates neutrino emission for a specific imaging geometry and setup. The results were overwritten into the suitably prepared data files of the originally empty user parameters of the hydrocode.

140 A series of imaging geometries were employed: No 1 means parallel rays, projected onto the XZ plane, no 2 the same but onto the YZ plane, no 3 is focused rays, onto the XZ plane, and no 4 is focused rays onto the YZ plane.

Parameter/Viewing Angle	0 deg	10 deg	30 deg	60 deg	D $\simeq$ 90 deg	Comments
cell size ( $\times 10^{10} cm$ )	2.0	2.0	2.0	2.0	2.0	PLUTO cell
$\rho_{jet}$ ( $cm^{-3}$ )	$1.0 \times 10^{10}$	$1.0 \times 10^{10}$	$1.0 \times 10^{10}$	$1.0 \times 10^{10}$	$1.0 \times 10^{10}$	jet's matter density
$\rho_w$ ( $cm^{-3}$ )	$1.0 \times 10^{13}$	$1.0 \times 10^{13}$	$1.0 \times 10^{13}$	$1.0 \times 10^{13}$	$1.0 \times 10^{13}$	max wind density
$\rho_{dw}$ ( $cm^{-3}$ )	$2.0 \times 10^{13}$	$2.0 \times 10^{13}$	$2.0 \times 10^{13}$	$2.0 \times 10^{13}$	$2.0 \times 10^{13}$	max disk wind density
$t_{run}^{max}$ (s)	842	842	842	842	842	model run time
Method	P. L.	P. L.	P. L.	P. L.	P. L.	Piecewise Linear
Integrator	M. H.	M. H.	M. H.	M. H.	M. H.	MUSCL-Hancock
EOS	Ideal	Ideal	Ideal	Ideal	Ideal	Equation of state
BinSep (cm)	$4.0 \times 10^{12}$	$4.0 \times 10^{12}$	$4.0 \times 10^{12}$	$4.0 \times 10^{12}$	$4.0 \times 10^{12}$	Binary separation
$M_{BH}/M_{\odot}$	3-10	3-10	3-10	3-10	3-10	VE compact star mass
$M_{\star}/M_{\odot}$	10-30	10-30	10-30	10-30	10-30	Companion mass
$\beta = v_0/c$	0.866	0.866	0.866	0.866	0.866	Initial jet speed
$L_k^p$	$2.5 * 10^{38}$	$2.5 * 10^{38}$	$2.5 * 10^{38}$	$2.5 * 10^{38}$	$2.5 * 10^{38}$	Jet kinetic luminosity
grid resolution	60*100*50	60*100*50	60*100*50	60*100*50	60*100*50	PLUTO grid size (xyz)
imaging method	FB	PR	PR	PR	FB	focused beam or parallel rays
time delay	off	off	off	off	off	very high LOS speed
imaging plane	XZ-screen	XZ/YZ	XZ/YZ	XZ/YZ	YZ-screen	box side or inner screen

Table 1: Table of run data

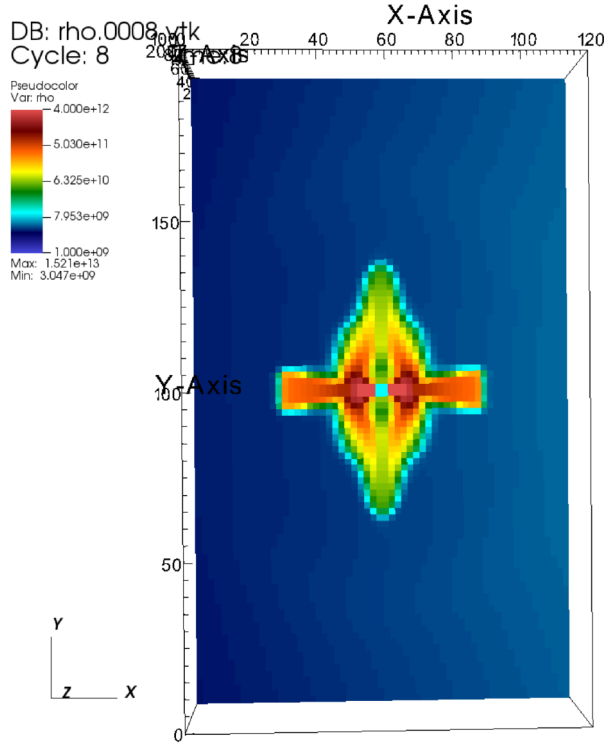


Figure 11: Snapshot 8 of the  $u=0.866c$  hydrocode run, corresponding to a model time of  $t=200$  ( $8 \times 25$ ), depicting a slice of the density in a logarithmic plot. The slice is cut along the jet. We can see both jet fronts traversing the stellar wind of the companion, after emerging from the model disk wind. Image produced with VisIt.

Three different angles were employed for the cases 1 and 2, while for cases 3 and 4 the respective focal points imply near-head-on and sidereal views.

145      Rlos2 [25] was then run, using the combined PLUTO-nemiss data, with  
 sfactor=1 for the pload shrink factor. In general, the imaging process may or  
 may not use all snapshots available to it, depending on the light crossing time  
 of its model segment (adjusted through the clight parameter in rlos2). Trying  
 to read more snapshots than loaded corrupts the hydrocode time array of rlos2,  
 150      called T, resulting to errors. For simplicity, in our case an artificially very  
 high clight was used, in order to effectively switch off the time-delay effect. A  
 double filter was used for velocity and for  $\cos u$  angle. A minimum velocity and  
 a maximum angle were set, in order to trigger the calculation of the neutrino  
 emission for a particular cell. This way, the expensive part of the simulation  
 155      was only performed where it was really worth it. This alleviated in part the  
 discrepancy between computational costs of the dynamic and the radiative parts

of the model.

An important aspect of this modelling approach is that each cell has a different emissivity visible from Earth, than its neighbors. That is because each cell  
160 may differ from the next one in terms of both speed and orientation to us. This combination means that, in general, the hydro model gives different results than the steady-state one. A vortex with relativistic velocities, for example, may in part appear very luminous, where it is fast with local speed pointing towards us, and also too dark, where velocities point away from us. In this simulation, such  
165 effects were limited, but at a higher resolution, it is expected than non-linear dynamic effects in the hydrocode shall interact profoundly with the radiative part of the model.

The scale of the total emission increases the closer the LOS gets to the jet pair axis Figures 12 and 13. The low resolution employed did not allow for significant  
170 non-linear dynamic effects to appear, yet the concept of the modelling process was proven to work in its entirety. On the other hand, the normalization process demonstrates the possibility of potential observations, as the results potentially fall within the detection range of contemporary arrays [5].

A series of both dynamical and imaging parameters may be adjusted, in order  
175 to cover different scenario. The suite works in a highly automated manner, and is prepared to take on high resolution applications. There, the relativistic effects of non-linear dynamics shall appear in full.

## 5. Final remarks

Particle emission from a typical microquasar was simulated using a suitable  
180 program suite. The results verified the integrity of the process, opening the way for more detailed runs in the future.

## References

- [1] I. F. Mirabel, L. F. Rodríguez, *Ann. Rev. Astron. Astrophys* 37 (1999) 409.



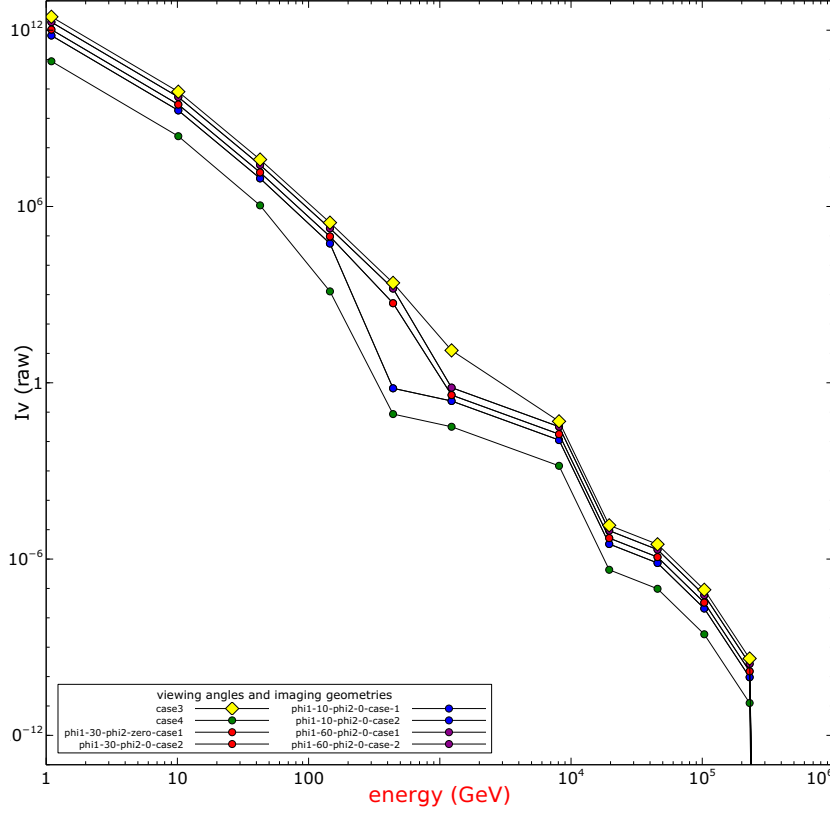


Figure 12: Non-normalized SED from a series of radiative simulations, based on the same RMHD dynamic model run. We can see the intensity dropping as the angle of observations deviates from the jet pair axis. Image produced with veusz, using data produced with PLUTO, rlos2 and nemiss.

- [2] G. E. Romero, D. F. Torres, M. M. Kaufman Bernadó, I. F. Mirabel, Hadronic gamma-ray emission from windy microquasars, *Astron. & Astrophys.* 410 (2003) L1–L4. [arXiv:astro-ph/0309123](#), [doi:10.1051/0004-6361:20031314-1](#).
- [3] W. Bednarek, TeV Neutrinos from Microquasars in Compact Massive Binaries, *Ap. J.* 631 (1) (2005) 466–470. [arXiv:astro-ph/0505547](#), [doi:10.1086/432411](#).
- [4] M. M. Reynoso, G. E. Romero, H. R. Christiansen, Production of gamma rays and neutrinos in the dark jets of the micro-

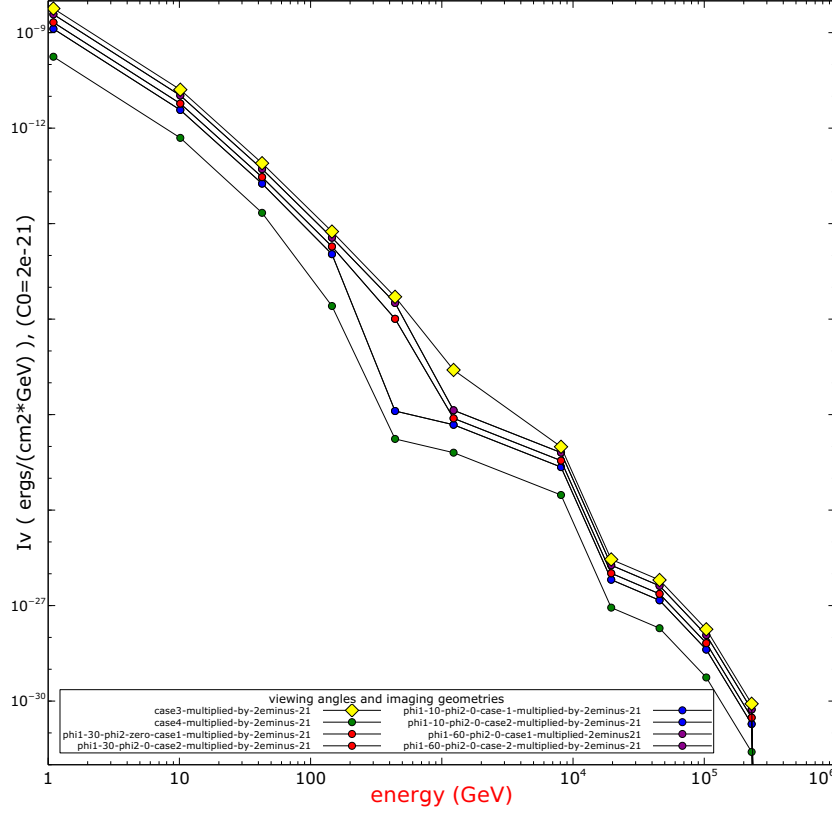


Figure 13: Normalized SED from a series of radiative simulations, where comparisons with potential observations are made possible. See the Appendix for more details on the normalization process. Data finally processed and image produced with `veusz`.

quasar SS433, MNRAS387 (4) (2008) 1745–1754. [arXiv:0801.2903](#),  
[doi:10.1111/j.1365-2966.2008.13364.x](#).

- [5] M. M. Reynoso, G. E. Romero, Magnetic field effects on neutrino production in microquasars, *Astron. & Astrophys.*493 (1) (2009) 1–11. [arXiv:0811.1383](#), [doi:10.1051/0004-6361:200811004](#).
- [6] M. M. Reynoso, A. M. Carulli, On the possibilities of high-energy neutrino production in the jets of microquasar SS433 in light of new observational data, *Astroparticle Physics* 109 (2019) 25–32. [arXiv:1902.03861](#),  
[doi:10.1016/j.astropartphys.2019.02.003](#).

- [7] D. Koessl, E. Mueller, W. Hillebrandt, Numerical simulations of axially symmetric magnetized jets. I - The influence of equipartition magnetic fields. II - Apparent field structure and theoretical radio maps. III - Collimation of underexpanded jets by magnetic fields, *Astron. & Astrophys.* 229 (2) (1990) 378–415.
- [8] F. M. Rieger, P. Duffy, A Microscopic Analysis of Shear Acceleration, *Ap. J.* 652 (2) (2006) 1044–1049. [arXiv:astro-ph/0610187](#), [doi:10.1086/508056](#).
- [9] F. M. Rieger, An Introduction to Particle Acceleration in Shearing Flows, *Galaxies* 7 (3) (2019) 78. [arXiv:1909.07237](#), [doi:10.3390/galaxies7030078](#).
- [10] Singh2019MHD, Study of relativistic magnetized outflows with relativistic equation of state, *Monthly Notices of the Royal Astronomical Society* 488 (4) (2019) 5713–5727. [arXiv:https://academic.oup.com/mnras/article-pdf/488/4/5713/29191239/stz2101.pdf](#), [doi:10.1093/mnras/stz2101](#).  
URL <https://doi.org/10.1093/mnras/stz2101>
- [11] S. Fabrika, The jets and supercritical accretion disk in SS433, 12 (2004) 1–152. [arXiv:astro-ph/0603390](#).
- [12] S. R. Kelner, F. A. Aharonian, V. V. Bugayov, Energy spectra of gamma rays, electrons, and neutrinos produced at proton-proton interactions in the very high energy regime, *Phys. Rev. D* 74 (3) (2006) 034018. [arXiv:astro-ph/0606058](#), [doi:10.1103/PhysRevD.74.034018](#).
- [13] P. Lipari, M. Lusignoli, D. Meloni, Flavor composition and energy spectrum of astrophysical neutrinos, *Physical Review D* 75 (12). [doi:10.1103/physrevd.75.123005](#).  
URL <http://dx.doi.org/10.1103/PhysRevD.75.123005>
- [14] M. C. Begelman, R. D. Blandford, M. J. Rees, Massive black hole

- binaries in active galactic nuclei, *Nature* 287 (5780) (1980) 307–309.  
 230 `doi:10.1038/287307a0`.
- [15] P. A. Hughes, in: Hughes (Ed.), *Beams and Jets in Astrophysics*, Cambridge University Press, 1991.
- [16] E. V. Derishev, F. A. Aharonian, V. V. Kocharovsky, High-energy emission from off-axis relativistic jets, in: F. A. Aharonian, H. J. Völk, D. Horns (Eds.), *High Energy Gamma-Ray Astronomy*, Vol. 745 of  
 235 *American Institute of Physics Conference Series*, 2005, pp. 510–515. `arXiv:astro-ph/0501197`, `doi:10.1063/1.1878454`.
- [17] O. Kosmas, T. Smponias, aHEP accepted (2018).
- [18] T. Smponias, O. Kosmas, *Advances in High Energy Physics* 4962741.
- 240 [19] T. Smponias, O. Kosmas, *Advances in High Energy Physics* 921757.
- [20] W. R. M. James J. Duderstadt, *Transport theory*, Wiley, New York, 1979.
- [21] T. Smponias, T. S. Kosmas, *MNRAS* 438 (2014) 1014.
- [22] T. Smponias, T. S. Kosmas, *MNRAS* 412 (2011) 1320.
- [23] D. F. Torres, A. Reimer, Hadronic beam models for quasars and microquasars, *Astron. & Astrophys.* 528 (2011) L2. `arXiv:1102.0851`,  
 245 `doi:10.1051/0004-6361/201116488`.
- [24] D. Purmohammad, J. Samimi, On the hadronic beam model of TeV gamma-ray flares from blazars, *Astron. & Astrophys.* 371 (2001) 61–67. `doi:10.1051/0004-6361:20010308`.
- 250 [25] T. Smponias, RLOS: Time-resolved imaging of model astrophysical jets (Nov. 2018). `arXiv:1811.009`.
- [26] T. Smponias, nemiss: neutrino imaging of model astrophysical jets (Nov. 2019).

## 6. Appendix 1

### 255 6.1. Normalization

The kinetic energy of the jet at its base can be expressed as

$$E_k = \frac{1}{2}(\Gamma m)u^2 \quad (22)$$

where  $u$  is the jet speed, and  $m$  the mass of a jet portion crossing the cross section of the jet there. Then, the jet kinetic power, is the kinetic energy traversing the cross section per unit time

$$P_k = dE_k/dt = \frac{1}{2}(\Gamma dm/dt)u^2 \quad (23)$$

where the speed is taken constant during an ejection episode (it is also set constant in the simulation described here). But

$$dm/dt = \rho dV/dt = \rho A dx/dt = \rho A u \quad (24)$$

where  $A$  is the jet base cross section area, also taken constant both in the simulation and here. Therefore

$$P_k = dE_k/dt = \frac{1}{2}(\Gamma \rho A)u^3 \quad (25)$$

or

$$P_k = dE_k/dt = \frac{1}{2}(\Gamma \rho N_{cell} L_{cell}^2)u^3 \quad (26)$$

where  $A = N_{cell} L_{cell}^2$ .  $L_{cell}^2$  is the area of the side of length  $L_{cell}$  of a cubical computational cell, at the jet base, and  $N_{cell}$  is the number of such cells forming the jet base. We then express density as a function of proton number density  $N_p$  and proton mass  $m_p$

$$\rho = N_p m_p. \quad (27)$$

Furthermore, we introduce a factor  $\alpha = L_\nu/L_k$ , representing the portion of jet power emitted in neutrinos. A typical value is taken as  $10^{-3}$ . We also set  $u=\beta c$ . A less than unity, positive filtering factor  $f_f$  is employed, which accounts for  
 260 not using all of the jet cells, but only those with velocity orientation closer to the LOS and also with speed above a given limit.

We then have

$$L_\nu = \alpha L_k = \alpha P_k = \alpha dE_k/dt = f_f \frac{1}{2} \alpha \Gamma (N_p m_p N_{cell} L_{cell}^2) \beta^3 c^3 \quad (28)$$

The intensity of the jet is then expressed as  $I_\nu = L_\nu / 4\pi D^2$ , where D is the distance to Earth. Thus

$$I_\nu = f_f \frac{1}{4\pi D^2} \alpha \frac{1}{2} \Gamma (N_p m_p N_{cell} L_{cell}^2) \beta^3 c^3 \quad (29)$$

In our simulation, the jet beam travels at  $\beta = \frac{u}{c} = 0.866$ , with a density of  $10^{10}$  protons/cm<sup>3</sup>.  $L_{cell}$  is  $10^{10}$  cm, while the number of cells comprising the beam, at its base, at this resolution, is  $N_{cell} \simeq 15$ .  $\Gamma = 2$ . The distance to Earth, is  
 265 taken here with a typical value of  $D = 5$  kpc, or approximately  $2 \times 10^{22}$  cm.

We then integrate the area under the curve of the arbitrary units plot, for the case of nearly non-beamed data, at  $\phi_1 = 10$  degrees. That case is supposed, for the purposes of normalization, to be the one matching the orientation of the hypothetical system in relation to Earth. We do a cumulative sum over the  
 270 roughly ten points, admitting a ten percent coverage per order of magnitude scale level. Thus, we find about  $10^{11}$ , which means that our sum is ten times smaller, or approximately  $10^{10}$ , in arbitrary units (AU)\*GeV. We replace an AU with a constant  $C_0$ , so that  $AU = C_0 \text{ erg}/(\text{s} \cdot \text{cm}^2)$ .

We set  $I_\nu = L_\nu / 4\pi D^2$  equal to the area under the plot, expressed in units of  $C_0$ , in order to find the latter (normalization constant)

$$I_\nu = f_f \frac{1}{4\pi D^2} \alpha \frac{1}{2} \Gamma (N_p m_p) N_{cell} L_{cell}^2 \beta^3 c^3 = (PLOTAREA) * C_0 \text{ erg}/(\text{s} \cdot \text{cm}^2) \text{ GeV} \quad (30)$$

For our case, we find  $C_0 \simeq 2 \cdot 10^{-21}$ , which is the value of the arbitrary unit  $C_0$ .  
 275 Using the above constant, we multiply by it the value given in arbitrary units for the particle emission. Thus the intensity plot is multiplied, and we arrive to the updated plot in Figure 13, which may be directly compared to other models and to observations.

## 7. Appendix 2

The equipartition calculation now follows. As shown above, the jet kinetic power is

$$L_k = \frac{1}{2} \frac{dm}{dt} u^2 = \frac{1}{2} (\rho Au) u^2 = \frac{1}{2} \rho A u^3 \quad (31)$$

where  $\frac{dm}{dt} = \rho \frac{dV}{dt} = \rho A \frac{dx}{dt} = \rho A u$

The kinetic energy density is [5]

$$\rho_k = \frac{L_k}{\pi R_j^2 u_j} = \frac{L_k}{Au} = \frac{\frac{1}{2} \rho A u^3}{Au} = \frac{1}{2} \rho u^2 \quad (32)$$

which also acts as verification.

We also have

$$B = \sqrt{8\pi\rho_B} \quad (33)$$

For equipartition, we set the kinetic and magnetic energy densities equal to each other,  $\rho_k = \rho_B$ . So

$$B = \sqrt{8\pi\rho_B} = \sqrt{8\pi\rho_k} \quad (34)$$

We can now have  $\rho_k$  and then we shall calculate the B that corresponds to equipartition for that. Our beam has  $\rho=10^{10}\text{cm}^{-3}$ , or about  $1.6 \times 10^{-14} \text{gcm}^{-3}$ .

So

$$\rho_k = \frac{1}{2} (1.6 \times 10^{-14} \frac{\text{g}}{\text{cm}^3}) (\frac{\sqrt{3}}{2} 3 \times 10^{10} \frac{\text{cm}}{\text{s}})^2 \simeq 5.4 \times 10^6 \frac{\text{g}}{\text{cm}^3} \quad (35)$$

Therefore, in CGS

$$B = \sqrt{8\pi\rho_k} \simeq \sqrt{8\pi \cdot 5.4 \times 10^6} \simeq 11.5 \times 10^3 \quad (36)$$

For our simulation we set a rounded value of  $B=10^4 \text{ G}$ , which is not far from the approximate equipartition value found above.